PENNSTATE

1855

IGNITION AND COMBUSTION CHARACTERISTICS OF METALLIZED PROPELLANTS

D. C. Mueller and S. R. Turns

Department of Mechanical Engineering
Propulsion Engineering Research Center
The Pennsylvania State University
University Park, PA 16802

TR-92-010

Annual Report (August 1991 - July 1992) to NASA Lewis Research Center
Grant No. NAG 3-1004

IGNITION AND COMBUSTION CHARACTERISTICS OF METALLIZED PROPELLANTS

Annual Report

(July 1991-July 1992)

Prepared by

D. C. Mueller and S. R. Turns

Department of Mechanical Engineering
and the
Propulsion Engineering Research Center
The Pennsylvania State University
University Park, PA 16802

for

NASA Lewis Research Center

Grant No. NAG 3-1044

Bryan Palaszewski
NASA Technical Officer

July 1991

Summary

During this reporting period, theoretical work on the secondary atomization process was continued and the experimental apparatus was improved. A one-dimensional model of a rocket combustor, incorporating multiple droplet size classes, slurry combustion, secondary atomization, radiation heat transfer, and two-phase slip between slurry droplets and the gas flow has been derived and a computer code has been written to implement this model. The STANJAN chemical equilibrium solver has been coupled with this code to yield gas temperature, density, and composition as functions of axial location. Preliminary results indicate that the model is performing correctly, given current model assumptions.

Radiation heat transfer in the combustion chamber is treated as an optically-thick participating media problem requiring a solution of the radiative transfer equation. A cylindrical $\overline{P}_1$ approximation has been employed to yield an analytical expression for chamber-wall heat flux at each axial location.

The code was exercised to determine the effects of secondary atomization intensity, defined as the number of secondary drops produced per initial drop, on chamber burnout distance and final Al_2O_3 agglomerate diameter. These results indicate that only weak secondary atomization is required to significantly reduce these two parameters. Stronger atomization intensities were found to yield decreasing marginal benefits.

The experimental apparatus was improved to reduce building vibration effects on the optical system alignment. This was accomplished by mounting the burner and the transmitting/receiving optics on a single frame supported by vibration-isolation legs. Calibration and shakedown tests indicate that vibration problems have been eliminated and that the system is performing correctly.

Table of Contents

OVERALL PROGRAM OBJECTIVES

The overall objective of this project is to provide an increased understanding of the secondary atomization characteristics of Al/RP-1 slurry propellants. Specific objectives are as follows:

1. Develop an experimental system to measure the size and velocity of burning 10-100 μm slurry droplets and to check for the presence of burning aluminum in these same droplets.

2. Use this experimental system to determine the ignition and secondary atomization characteristics of various slurry formulations.

3. From the experimental data develop an understanding of the role surfactants, gellants, and ultimate particle play in the secondary atomization process.

4. Develop analytical models of droplet ignition and secondary atomization.

5. Apply these models in a 1-D rocket model to determine the effects of secondary atomization on engine performance.

PROGRESS DURING REPORTING PERIOD

THEORETICAL EFFORTS

One Dimensional Rocket Model

Recent performance analyses of slurry fueled rockets[1-5] predict that Al slurry propellants may increase maximum payload over neat liquid systems. However, these studies neglect additional radiation and two-phase flow losses resulting from solid combustion products and increases in droplet combustion times due to solid agglomerate combustion. Accounting for these three factors is critical in accurately predicting the effects of using metallized propellants as rocket fuels.

Our previous research involving slurry droplet combustion[6-7] focused on the mechanism of secondary atomization as a possible means of reducing combustion times and two-phase flow losses. However, this research was devoted to understanding the droplet combustion and secondary atomization processes themselves and did not involve the effects of secondary atomization on engine performance.

Consequently, a one-dimensional engine model is being derived to provide a preliminary evaluation of the effects of secondary atomization, two-phase flow losses, and radiation heat transfer on engine performance. Coding a new model provides some benefits over using a standard code such as TDK. First, the new model will permit the inclusion of secondary atomization effects, and second, the model will allow a clearer, if simpler, understanding of the physics involved in the problem.

Over the past six months, a numerical code incorporating the following effects has been written to model a rocket combustion chamber:

- Multiple droplet size classes
- Gas-phase chemical equilibrium

- Two-phase flow losses
- Hydrocarbon evaporation and burnout
- Al combustion with surface condensation of Al_2O_3
- Simple secondary atomization

Chamber dimensions and propellant flow rates have been taken from Galecki's work[8] to provide realistic model inputs.

Model Description

The propellants used in the engine model are a JP-10/Al slurry and a preheated gaseous O_2 oxidizer. JP-10, a pure hydrocarbon ($C_{10}H_{16}$), was chosen as the slurry hydrocarbon component instead of RP-1 to avoid the complexity of modeling multi-component droplet combustion.

The combustor flow is modeled using a single product-phase containing both gases and small Al_2O_3 fume particles, and three additional flow phases for each droplet size class: a liquid hydrocarbon phase, an aluminum phase, and a phase containing large Al_2O_3 agglomerates. The Al_2O_3 must be separated into two flow phases because of the two oxidation mechanisms inherent in aluminum combustion.[9-11] In the first oxidation mechanism, large Al_2O_3 agglomerates are formed through droplet surface condensation/oxidation, and in the second, very small Al_2O_3 fume particles are produced through vapor-phase oxidation. Since the Al_2O_3 agglomerates are much larger than the fume particles and are attached to the surface of the aluminum droplets it is necessary to model the Al_2O_3 agglomerates separately from the fume particles. Including the fume particles in the gas-phase flow requires the assumptions of no temperature or velocity slip between the fume particles and the gases, but greatly simplifies the problem solution.

As an Al droplet burns, it continually produces Al_2O_3 fume particles at the oxide boiling point which subsequently equilibrate with the gas-phase temperature and velocity.

This process results in a range of fume particle temperatures and velocities as new particles are created and older particles continue to equilibrate with the gases. If the temperature and velocity slip were not neglected, many additional flow phases would be required to accurately model this range of fume particle temperatures and velocities.

Verification of No Slip Assumptions

Al_2O_3 fume particles formed during aluminum combustion in a rocket environment are typically on the order of one micron in size.[9-12] Parry and Brewster[12] measured a fume particle mean diameter, D_{32}, of 0.97 μm. Using the model for particle acceleration developed later in this report, it was found that these fume particles rapidly accelerate to the gas-phase velocity thus justifying the no-slip velocity condition.

The no-slip temperature condition requires that the convective heat transfer resistance be much less than the radiation heat transfer resistance for a minimal temperature difference between the steady-state particle and gas temperatures. The combined radiation/convection heat transfer rate must also be large enough to allow particle temperature, T_p, to rapidly adjust to a changing gas temperature, T_{gas}. The following is an analysis verifying the no slip temperature condition, which is defined as:

$$\left|T_{gas} - T_p\right| \leq 0.01 T_{gas} \quad . \qquad (1)$$

At equilibrium, the energy radiated from an Al_2O_3 particle to the surrounding medium equals that convected to the particle from the gas flow. However, the solution of a participating medium radiation problem is complex with radiant intensity dependent on particle location in the chamber. As a conservative approximation, medium participation is neglected and the fume particles are assumed to radiate directly to the chamber walls. Using this approximation, the particle energy balance can be expressed as

$$Ah\left(T_{gas} - T_p\right) = A\varepsilon\sigma\left(T_p^4 - T_w^4\right) \quad . \tag{2}$$

where A is the particle surface area; h, the convective heat transfer coefficient; ε, the particle emissivity; and σ, the Stefan-Boltzmann constant. The wall temperature in the radiation term, T_w, is an unknown parameter dependent on chamber cooling design but is typically much less than the oxide fume temperature and can therefore be neglected. Substituting for h using the definition of the Nusselt number

$$Nu = \frac{hD_p}{k_{gas}} \quad , \tag{3}$$

where D_p is particle diameter, and for T_p using the no-slip definition, yields

$$\frac{Nu\, k_{gas}}{D_p}\left(T_{gas} - 0.99T_{gas}\right) = \varepsilon\sigma\left(0.99T_{gas}\right)^4. \tag{4}$$

Equation 4 can be simplified to yield the maximum gas temperature, above which, the no-slip temperature condition is invalid. This yields

$$T_{gas,max} = \sqrt[3]{0.0104\frac{Nu\, k_{gas}}{D_p\, \varepsilon\sigma}} \quad . \tag{5}$$

The fume particles can be modeled as spheres in a stagnant environment by employing the no-slip velocity condition, yielding a Nusselt number of 2.0. The fume particles can be approximated as uniform 0.97 μm diameter spheres and the gas

conductivity, k_{gas}, as that of oxygen (k = 0.215 W/m·K at 4000 K).[13] Konopka, Reed, and Calia[14] report that impurities can influence the infrared optical properties of Al_2O_3 particles produced by solid rocket motors and that these optical properties can vary from engine to engine. Because of this uncertainty, a particle emissivity of 1.0 is used as an extreme value.

Using the above assumptions in Eq. 5, a maximum allowable gas temperature of approximately 4330 K is calculated. Currently, the chamber model is adiabatic, predicting a worst-case maximum temperature of 3872 K. Accounting for flow heat losses, a participating medium and using a fume particle emissivity less than 1.0 should increase this difference even more, clearly indicating that the steady-state fume particle temperature is close to the gas temperature for a constant gas temperature situation.

The fume particle temperature must also respond quickly to changes in the gas temperature for the no-slip temperature condition to apply. This second requirement is verified as follows:

Approximating the fume particles as uniform temperature spheres requires that the Biot-number criterion be satisfied.

$$\mathrm{Bi} = \frac{hL_c}{k_{Al_2O_3}} < 0.1 \quad \text{where} \quad L_c \equiv \frac{D_p}{6} \quad . \tag{6}$$

Assuming a spherical particle moving at the gas-phase velocity, the Biot number reduces to

$$\mathrm{Bi} = \frac{1}{3}\frac{k_{gas}}{k_{Al_2O_3}} \quad , \tag{7}$$

where k is thermal conductivity. The minimum thermal conductivity of Al_2O_3 (~5.66 W/m·K at 1500 K)[15] and the maximum gas thermal conductivity (~ 0.22 W/m·K for O_2 at 4000 K)[13] were used in estimating the maximum Biot number. This results in Bi ≈ 0.01, indicating that Al_2O_3 fume particles can be modeled using a lumped-temperature analysis.

Based on the above lumped-temperature approximation, the change in sensible energy of a particle can be determined through the unsteady energy equation,

$$mc_p \frac{dT_p}{dt} = -A\left[h\left(T_p - T_{gas}\right) + \varepsilon\sigma\left(T_p^4 - T_w^4\right)\right] \quad , \tag{8}$$

where m is the mass of an Al_2O_3 fume particle; c_p, the specific heat of Al_2O_3; and A, the particle surface area. Given an initial particle temperature, $T_{p,init}=0.99T_{gas,init}$, and a new gas temperature, $T_{gas,new}$, the time required for the particle temperature to reach $0.99T_{gas,new}$ can be determined by numerically integrating Eq. 8. If this particle response time is less than the time required for combustion to raise the chamber gas temperature from $T_{gas,init}$ to $T_{gas,new}$, then the no-slip temperature condition is valid for all times. Using the following approximate values, ρ_p= 3970 kg/m^3, D_p = 0.97 μm, c_p = 1225 J/kg·K, Nu = 2.0, ε = 1.0, and k_{gas} = 0.2 W/m·K, yields a particle response time of 5.5 μs for a sudden jump in gas temperature from 3000 K to 3300 K. In comparison, model calculations predict that 250 μs are required for chamber gas temperature to rise from 3000 K to 3300 K indicating that particle response time is short enough for the no-slip temperature condition to apply.

Governing System Equations

Mass Conservation: For M droplet size classes, the following equation can be written for system mass conservation assuming steady-state conditions and that no mass is added to or removed from the chamber except at the injector face and the chamber exit:

$$\frac{d\dot{m}_{gas}}{dx} = -\sum_{j=1}^{M}\left(\frac{d\dot{m}_{LH}}{dx} + \frac{d\dot{m}_{Al}}{dx} + \frac{d\dot{m}_{Al_2O_3}}{dx}\right)_j \quad . \tag{9}$$

In Eq. 9, x is axial position in the combustor; j, a particular droplet size class; and $\dot{m}_{gas}$, the gas mass flux. The liquid hydrocarbon, aluminum, and Al_2O_3 agglomerate mass fluxes for a particular droplet size class are given as $\dot{m}_{LH}$, $\dot{m}_{Al}$, and $\dot{m}_{Al_2O_3}$, respectively. The terms on the right hand side of Eq. 9 are found from a hydrocarbon droplet gasification model and an aluminum droplet combustion model. The development of all three terms is similar and is presented below.

The change in mass of a single slurry droplet in a size class, j, during a time interval dt is:

$$m_{change,j} = \frac{dm_{drop,j}}{dt}dt \tag{10}$$

where $m_{change,j}$ represents the hydrocarbon, aluminum, or Al_2O_3 mass change. The value of $dm_{drop,j}/dt$ for the liquid hydrocarbon is found from the hydrocarbon gasification model while $dm_{drop,j}/dt$ for the aluminum and Al_2O_3 are both determined from the aluminum combustion model. Relating dt to dx through the chain rule and the velocity relationship

$$u_{p,j} = \frac{dx}{dt} \tag{11}$$

yields

$$m_{change,j} = \frac{dm_{drop,j}}{dt}\frac{dx}{u_{p,j}} \quad , \tag{12}$$

where $u_{p,j}$ is the velocity of droplets in the j^{th} size class. This velocity is calculated through a drag analysis developed later in the report.

Equation 12 can be converted to a change in mass flux by multiplying $m_{change,j}$ by the total number of droplets in the j^{th} size class passing through the control volume per unit time, N/τ_j. Substituting this result, Eq. 9 becomes

$$\frac{d\dot{m}_{gas}}{dx} = -\sum_{j=1}^{M}\left[\left.\frac{N}{\tau}\right|_j \frac{1}{u_{p,j}}\left\{\left(\frac{dm_{drop}}{dt}\right)_{LH} + \left(\frac{dm_{drop}}{dt}\right)_{Al} + \left(\frac{dm_{drop}}{dt}\right)_{Al_2O_3}\right\}_j\right] \quad . \tag{13}$$

The value of N/τ_j for each droplet size class can be determined from the total initial slurry mass flux and normalized droplet size distribution. Given an initial normalized droplet size distribution, it is necessary to determine N/τ_{total} before N/τ_j can be found for the individual size classes. N/τ_{total} can be found from the following mass conservation expression:

$$\dot{m}_{slurry,initial} = \left.\frac{N}{\tau}\right|_{total} \sum_{j=1}^{n}\left(\tilde{N}_j \frac{1}{6}\rho\pi d_{j,init}^3\right) \quad , \tag{14}$$

where $\tilde{N}_j$ represents the percentage of total droplets in a given size class, given by the normalized size distribution. The variables, $d_{j,init}$ and ρ, represent the initial diameter of

the j^{th} size class and the initial slurry density, respectively. With N/τ_{total} known, N/τ_j for each size class can be calculated from

$$\left.\frac{N}{\tau}\right|_j = \tilde{N}_j \left.\frac{N}{\tau}\right|_{total} \quad . \tag{15}$$

Neglecting droplet breakup and secondary atomization, N/τ_j is constant throughout the chamber. This leaves the following three variables for each size class to be determined from the droplet gasification models: $\left(dm_{drop,j}/dt\right)_{LH}$, $\left(dm_{drop,j}/dt\right)_{Al}$, $\left(dm_{drop,j}/dt\right)_{Al_2O_3}$.

Energy Conservation: The steady-state energy balance for the system, including radiation heat losses, can be expressed as

$$\frac{d(\dot{m}h)_{gas}}{dx} = -\sum_{j=1}^{j=n}\left[\frac{d(\dot{m}h)_{LH}}{dx} + \frac{d(\dot{m}h)_{Al}}{dx} + \frac{d(\dot{m}h)_{Al_2O_3}}{dx}\right]_j - q^r \quad , \tag{16}$$

where h represents total specific enthalpy ($h_{chem} + h_{sens}$) and q^r is the radiation heat flux from the flow to the wall. Since gas flow optical properties are dominated by the small Al_2O_3 fume particles[12], the radiation term is independent of the individual droplet size classes and is not included in the summation term.

Each of the bracketed terms on the right hand side of Eq. 16 can be expanded as

$$\left.\frac{d(\dot{m}h)}{dx}\right|_j = \left[\dot{m}\frac{dh}{dx} + h\frac{d\dot{m}}{dx}\right]_j \quad . \tag{17}$$

Substituting for dm/dx yields

$$\left.\frac{d(\dot{m}h)}{dx}\right|_j = \left[\dot{m}\frac{dh}{dx} + h\left(\frac{N}{\tau}\frac{1}{u_p}\frac{dm_{drop}}{dt}\right)\right]_j \quad . \tag{18}$$

Because the enthalpy required to heat the liquid hydrocarbon from 300K to the hydrocarbon boiling temperature (438.9 kJ/kg at P = 6 atm) is comparable to the hydrocarbon latent heat of vaporization (~286.7 kJ/kg at P = 6 atm), hydrocarbon heatup must be accounted for in the hydrocarbon vaporization model developed later in this report. In the vaporization model, the bulk droplet temperature is assumed to remain at the initial droplet temperature. Heat transfer from the gas heats a thin surface layer of liquid hydrocarbon from the initial temperature to the boiling point and vaporizes this hydrocarbon layer. Using the constant bulk droplet temperature assumption yields a constant liquid hydrocarbon specific enthalpy, which reduces Eq. 18 for the liquid hydrocarbon to

$$\left.\frac{d(\dot{m}h)_{LH}}{dx}\right|_j = h_{LH,T_{init}}\left[\frac{N}{\tau}\frac{1}{u_p}\frac{dm_{drop,LH}}{dt}\right]_j \quad , \tag{19}$$

where $h_{LH,Tinit}$ is the liquid hydrocarbon specific enthalpy at the initial droplet temperature.

Following hydrocarbon burnout, an agglomerate of aluminum particles remains.[16,17] The aluminum agglomerate temperature rises from the hydrocarbon boiling temperature, through the aluminum melting point, to the aluminum boiling temperature as heat is transferred from the gas flow to the agglomerate. The enthalpy required for this temperature increase is significant compared to the total system enthalpy and the aluminum enthalpy of vaporization, $h_{fg,Al}$. Consequently, agglomerate ignition/heat up should be modeled. Presently, details of the agglomerate ignition/heat up process itself are

neglected but the enthalpy transfer required by the process is not. Upon hydrocarbon burnout, the aluminum agglomerate temperature is assumed to jump immediately to the aluminum boiling point, and the enthalpy required for this temperature jump is subtracted from the gas flow enthalpy.

Approximating the agglomerate ignition/heat up process as a step change significantly underpredicts droplet combustion times and is intended only as a temporary measure until other aspects of the code have been developed. Following this development, an aluminum agglomerate heat-up model will be incorporated into the code. After the step heat-up, Eq. 18 for the aluminum mass flux becomes

$$\left.\frac{d(\dot{m}h)_{Al}}{dx}\right|_j = h_{Al,T_{b,Al}}\left[\frac{N}{\tau}\frac{1}{u_p}\frac{dm_{drop,Al}}{dt}\right]_j , \qquad (20)$$

where $h_{Al,T_{b,Al}}$ is the liquid aluminum specific enthalpy at the boiling temperature.

Since Al_2O_3 agglomerate forms on the aluminum droplet surface, the Al_2O_3 agglomerate is maintained at the aluminum boiling temperature as long as any aluminum remains in the droplet. Ignoring the time period after aluminum burnout when Al_2O_3 agglomerate temperature can vary, Eq. 18 reduces to

$$\left.\frac{d(\dot{m}h)_{Al_2O_3}}{dx}\right|_j = h_{Al_2O_3,T_{b,Al}}\left[\frac{N}{\tau}\frac{1}{u_p}\frac{dm_{drop,Al_2O_3}}{dt}\right]_j \qquad (21)$$

for the Al_2O_3 agglomerate, where $h_{Al_2O_3,T_{b,Al}}$ is the Al_2O_3 specific enthalpy at the aluminum boiling temperature. Substituting Eqns. 19, 20 and 21 into Eq. 16 yields the final system energy balance:

$$\frac{d(\dot{m}h)_{gas}}{dx} = -\sum_{j=1}^{j=n} \frac{N}{\tau}\bigg|_j \frac{1}{u_{p,j}} \left[h_{LH,T_{init}} \frac{dm_{drop,LH}}{dt} + h_{Al,T_{b,Al}} \frac{dm_{drop,Al}}{dt} + h_{Al_2O_3,T_{b,Al}} \frac{dm_{drop,Al_2O_3}}{dt} \right]_j - q^r \quad . \quad (22)$$

Radiation Heat Transfer: Radiation from the solid combustion products to the chamber wall is a participating medium phenomena requiring the solution of the radiative-transfer equation. Expressed in cylindrical coordinates, this equation is

$$\sin\theta \left[\cos\phi \frac{\partial I(r,\theta,\phi)}{\partial r} - \frac{\sin\phi}{r} \frac{\partial I(r,\theta,\phi)}{\partial \phi} \right] + I(r,\theta,\phi) = (1-\Omega_0) I_{b,p}(r) + \frac{\Omega_0}{4\pi} \int_0^{2\pi} \int_0^{\pi} I(r,\theta',\phi') \sin\theta' d\theta' d\phi' \quad , \quad (23)$$

where $I(r,\theta,\phi)$ is the radiation intensity, r is radial distance from the centerline, and the variables, θ and ϕ, represent the angular spherical coordinates. $I_{b,p}(r)$ is the blackbody radiation emitted by the fume particles, and Ω_0 is the scattering albedo, defined as

$$\Omega_0 = \frac{\sigma_s}{a + \sigma_s} \quad (24)$$

where a and σ_s are the absorption and scattering coefficients, respectively. The absorption and scattering coefficients are currently unknown properties that must be determined before the transfer equation can be solved.

Given a scattering albedo, the transfer equation can be solved numerically, but requires a great deal of computer time. Fortunately, the transfer equation can be simplified and solved using one of several approximations based on the value of the optical thickness, K_D, which is defined as

$$K_D = \int_0^S (a + \sigma_s) ds = \int_0^S \kappa ds \quad , \tag{25}$$

where S is the characteristic radiation path length. If κ, defined as $(a + \sigma_s)$, is constant along this path, K_D can be expressed as

$$K_D = \kappa S \quad . \tag{26}$$

Al_2O_3 smoke optical properties are used in evaluating the transfer equation since the smoke particles dominate the gas flow optical properties as discussed earlier in the report. Parry and Brewster[12] determined the optical properties of Al_2O_3 smoke produced by a solid propellant containing 20% aluminum by mass, burning at a 1.8 MPa pressure. Optical thicknesses, K_D = 1.28 at λ = 632.8 nm and K_D = 1.21 at λ = 1064 nm, were found for the 1 mm thick smoke region. Assuming a constant κ in the transmission direction, Eq. 26 produces κ = 1280 and κ = 1210 for λ_1 and λ_2, respectively.

Although the above κ values were obtained from a solid propellant flame, they should provide a first approximation of the gas flow optical thickness in the model combustion chamber. Given that κ is a function of fume volume fraction, κ actually may be greater for aluminum slurry combustion than for the above solid propellant due to the higher slurry aluminum mass percentage. As a conservative estimate, Parry and Brewsters' κ values will be used in estimating a minimum gas flow optical thickness.

In the model, chamber radius, R = 0.025 m, is the characteristic path length. Using this radius, the optical thickness is between 30 and 32. These values are much greater than K_D = 2.0, which is considered the lower limit for an optically-thick medium.[18] Therefore, as a first estimate, the gas flow can be treated as an optically-thick medium, in which local radiation heat transfer is only influenced by the immediate surroundings .

Based on this optical thickness, a diffusion approximation[18] can be used to simplify the radiative transfer equation.

The cylindrical P_1 diffusion approximation[19] has been chosen since it provides greater accuracy than other approximations, yet is still simple to incorporate. In the P_1 approximation, the radiant intensity is treated as a series expansion,

$$I(r,\theta,\phi) = \sum_{n=0}^{\infty} \sum_{m=-n}^{n} Y_{nm}(\theta,\phi)\, \Psi_{nm}(r) \quad , \tag{27}$$

where $\Psi_{nm}(r)$ are unknown functions, and $Y_{nm}(\theta,\phi)$ are defined as

$$Y_{nm}(\theta,\phi) = (-1)^m \sqrt{\frac{(n-m)!}{(n+m)!}}\, P_n^m(\cos\theta)\, e^{im\phi} \quad . \tag{28}$$

In Eq. 28, $P_n^m(\cos\theta)$ are Legendre polynomials and $i = \sqrt{-1}$.

Eq. 27 is substituted into the transfer equation (Eq. 23) and the resulting equation is then mathematically manipulated, yielding the following expression:

$$\sum_{n=0}^{\infty} \sum_{m=-n}^{n} Y_{nm}(\theta,\phi) \left\{ A_{nm} \left[\frac{d\Psi_{n+1,m+1}(r)}{dr} + \frac{m+1}{r} \Psi_{n+1,m+1}(r) \right] - B_{nm} \left[\frac{d\Psi_{n+1,m-1}(r)}{dr} - \frac{m-1}{r} \Psi_{n+1,m-1}(r) \right] \right.$$
$$- C_{nm} \left[\frac{d\Psi_{n-1,m+1}(r)}{dr} + \frac{m+1}{r} \Psi_{n-1,m+1}(r) \right] + D_{nm} \left[\frac{d\Psi_{n-1,m-1}(r)}{dr} - \frac{m-1}{r} \Psi_{n-1,m-1}(r) \right]$$
$$\left. + \Psi_{nm}(r) - \left[(1-\Omega_0) I_b(r) + \Omega_0 \Psi_{00} \right] \delta_{0n} \delta_{0m} \right\} = 0 \quad , \tag{29}$$

where δ_{ij} is the Kronecker delta. Since $Y_{nm}(\theta,\phi)$ does not equal zero, the expression in the { } brackets must equal zero for all n and m.

Assuming that the radiant intensity is axisymmetric about the chamber centerline ($I(r,\theta,\phi) = I(r,\theta,-\phi)$), and that the radiant intensity does not vary along the chamber centerline ($I(r,\theta,\phi) = I(r,\pi-\theta,\phi)$), Eq. 29 yields a set of N+1 coupled equations where the number of equations is related to the order of the approximation; i.e. n=0,1,...,N . In the P_1 approximation, this series is terminated at N=1, resulting in the following two coupled equations:

$$\frac{d^2\Psi_{0,0}(r)}{dr^2}+\frac{1}{r}\frac{d\Psi_{0,0}(r)}{dr}-3(1-\Omega_0)\Psi_{0,0}(r)=-3(1-\Omega_0)I_{b,p}(r) \quad , \qquad (30)$$

and

$$\frac{d\Psi_{0,0}(r)}{dr}+\sqrt{2}\Psi_{1,1}(r)=0 \quad , \qquad (31)$$

where $I_{b,p}(r)$ is the blackbody intensity emitted by the fume particles. Since the combustor model is one dimensional, particle temperature is independent of r; therefore $I_{b,p}(r)$ is independent of r.

The physical significance of $\Psi_{0,0}(r)$ and $\Psi_{1,1}(r)$ can be found from the definitions of incident radiation, G(r), and net radiative heat flux, $q^r(r)$, respectively. The incident radiation is defined as

$$G(r)=\int_{\phi=0}^{2\pi}\int_{\theta=0}^{\pi} I(r,\theta,\phi)\sin\theta\, d\theta\, d\phi \quad . \qquad (32)$$

Substituting the P_1 series expansion for $I(r,\theta,\phi)$ and integrating yields

$$\Psi_{0,0} = \frac{G(r)}{4\pi} \quad . \tag{33}$$

Similarly, the definition of net radiative heat flux,

$$q^r(r) = \int_{\phi=0}^{2\pi} \int_{\theta=0}^{\pi} I(r,\theta,\phi) \sin^2\theta \cos\phi \, d\theta d\phi \quad , \tag{34}$$

results in the following expression for $\Psi_{1,1}$:

$$\Psi_{1,1}(r) = -\frac{3}{\sqrt{2} \cdot 4\pi} q^r(r) \quad . \tag{35}$$

Replacing $\Psi_{0,0}$ and $\Psi_{1,1}$ in Eq. 30 and 31 produces the following system of radiative transfer equations:

$$\frac{d^2G(r)}{dr^2} + \frac{1}{r}\frac{dG(r)}{dr} - 3(1-\Omega_0)G(r) = -12\pi(1-\Omega_0)I_{b,p} \tag{36}$$

$$\frac{dG(r)}{dr} + 3q^r(r) = 0 \quad . \tag{37}$$

Equation 36 can be solved for G(r) given the appropriate boundary conditions, and Eq. 37 can be solved for $q^r(r)$ using the solution for G(r). Using the fact that G(r) is axisymmetric about the centerline (r=0) and assuming that the chamber wall (r=R) behaves as a blackbody, the boundary conditions can be expressed as

$$\frac{dG(0)}{dr} = 0 \tag{38a}$$

$$G(R) + \frac{2}{3}\frac{dG(R)}{dr} = 4\pi I_{b,wall} \quad . \tag{38b}$$

Equation 36 can be transformed to a modified zero-order Bessel equation by using the variable substitution

$$\delta = \frac{r}{\xi} \quad \text{where} \quad \xi \equiv \frac{1}{\sqrt{3(1-\Omega_0)}} \quad . \tag{39}$$

Using this substitution and integrating Eq. 36 subject to the boundary conditions, the following expression for incident radiation is obtained:

$$G(r) = 4\pi I_{bf} + \frac{4\pi(I_{bw} - I_{bf})I_0\left(r/\xi\right)}{\left[I_0\left(R/\xi\right) + \frac{2}{3\xi}I_1\left(R/\xi\right)\right]} \quad . \tag{40}$$

$I_0(mr)$ and $I_1(mr)$ are the modified Bessel functions

$$I_\nu(mr) = \sum_{k=0}^{\infty} \frac{(mr/2)^{2k+\nu}}{k!\Gamma(k+\nu+1)} \quad , \tag{41}$$

where ν equals 0 or 1 and $m = 1/\xi$. Substituting Eq. 40 into Eq. 37, the following expression for $q^r(r)$ is obtained:

$$q^r(r) = \frac{4\pi\sigma\left(T_{gas}^4 - T_{wall}^4\right) I_1\left(r/\xi\right)}{\left[3\xi I_0\left(R/\xi\right) + 2I_1\left(R/\xi\right)\right]} \quad . \tag{42}$$

As mentioned above, the absorption and scattering coefficients, σ_a and σ_s, are still unknown and must be determined prior to solving for $q^r(r)$. Consequently, radiation heat transfer is currently neglected in the system energy balance (Eq. 22) but will be included upon successful determination of σ_a and σ_s.

Momentum Conservation: The gas-phase momentum equation in the combustion chamber is trivial, assuming a negligible chamber pressure gradient and no body forces. The negligible chamber pressure gradient condition should be accurate for current conditions, but does require the assumption of no wall frictional losses or pressure drops due to flow acceleration. However, the momentum equations governing the hydrocarbon, aluminum, and agglomerate Al_2O_3 mass fluxes are significant. In a given slurry droplet, there is no slip between the hydrocarbon and the aluminum before hydrocarbon burnout, and no slip between the aluminum and the Al_2O_3 agglomerate afterwards; therefore the hydrocarbon, aluminum and Al_2O_3 agglomerate momentum equations in a given droplet size class can be reduced to a single momentum equation. Virtual mass and Bassett forces can be neglected since the particle density is much greater than the gas density. The particle momentum equation for a droplet size class can be expressed as

$$\bar{\mathbf{F}} = m\bar{\mathbf{a}} \quad , \tag{43}$$

where **F** is the drag force on a particle, m is the particle mass and **a** is the particle acceleration, du_p/dt. Substituting for the drag force using a drag coefficient, C_D, and using the chain rule to relate du_p/t to du_p/dx results in the following form of Eq. 43:

$$\frac{du_p}{dx} = \frac{3}{4}\frac{\rho_{gas} C_D (u_g - u_p)|u_g - u_p|}{\rho_p d\, u_p} \quad (44)$$

In this equation, ρ_{gas} is the gas density, u_g the gas velocity, u_p the droplet velocity, ρ_p the droplet density, and d the droplet diameter.

The drag coefficient is approximated as that of a sphere using the following correlation[20]:

$$C_D = \frac{24}{Re} + \frac{6}{\left(1+\sqrt{Re}\right)} + 0.4 \quad , \quad (45)$$

where the Reynolds number, Re, is based on the slip velocity between the gas and the droplet.

Slurry Combustion Overview: The physics of slurry droplet combustion and a probable secondary atomization process are described in detail in other research.[6,7,16,17,21,22] In brief, when a slurry droplet is exposed to a hot ambient environment, heat transfer from the gas flow causes liquid hydrocarbon to vaporize and the droplet surface to regress. As liquid hydrocarbon vaporizes at the droplet surface, the aluminum particles that were suspended in the now vaporized hydrocarbon remain behind at the droplet surface, causing the number density of aluminum particles at the droplet surface to increase.

If the initial droplet is large enough, and there is a sufficient number of aluminum particles in the droplet, the number density of aluminum particles at the surface will increase until a rigid shell is formed by the particles coming into contact with each other. Some time interval after this rigid shell formation, surfactant pyrolysis causes the shell to become impermeable, and hydrocarbon vaporization to cease. Heat transfer to the slurry droplet continues, causing droplet internal pressure and rigid shell stresses to rise until the shell fails. Shell failure shatters the droplet, producing a number of smaller droplets which might repeat this secondary atomization process if the new droplets meet the minimum criteria for rigid shell formation.[7,21]

After hydrocarbon burnout occurs in a droplet or droplet fragment, the remaining agglomerate of aluminum particles heats up, melts to form a single molten aluminum droplet, and burns.

Secondary Atomization Modeling: Cho and Takahashi's shell formation model[21] is used to predict the droplet diameter at which rigid shell formation occurs for each droplet size class in the combustor model. When running the combustor code, it is assumed that secondary atomization occurs when the droplet diameter reaches the predicted rigid-shell diameter. Although secondary atomization actually occurs some time after rigid shell formation, the time interval presently is not known and is therefore neglected in the engine model. However, future experimental efforts should provide an estimate of this time interval, and then the time interval will be included in the engine model.

Particle size distribution after secondary atomization is also currently an unknown to be determined from experimental measurements and is treated as a system variable. In the combustor model, a droplet undergoing secondary atomization is presently assumed to shatter into a specified number of equal-size secondary droplets. Defining the fragmentation ratio, β, as the number of secondary droplets produced per initial droplet, a new value of N/τ_j can be expressed as

$$\left.\frac{N}{\tau}\right|_{j,new} = \beta \left.\frac{N}{\tau}\right|_{j,old} \quad . \tag{46}$$

Knowing the slurry mass flux of a given size class, $\dot{m}_{slurry,j}$, a new size class droplet diameter, $d_{j.new}$, can be found from the mass conservation expression,

$$\dot{m}_{slurry,j} = \left.\frac{N}{\tau}\right|_{j,new} \frac{\pi}{6} d^3_{j,new} \quad . \tag{47}$$

Hydrocarbon Vaporization: Because of the close proximity of the slurry droplets to each other, the droplets are not surrounded by individual flames. Therefore, droplet combustion can be modeled as an evaporation process. Droplet heat up is approximated by assuming that heat transfer from the gas flow only affects a thin layer of liquid at the droplet surface. All of the heat transferred to the droplet from the gas flow is consumed in heating the thin surface layer from the initial droplet temperature to the liquid boiling point and vaporizing the layer. Consequently, the bulk droplet temperature remains at the initial droplet temperature. Assuming the following:

- Quasi-steady droplet evaporation
- Lewis number, Le = 1
- Uniform droplet temperature equal to initial droplet temperature
- Constant thermophysical properties,

the gas-phase energy equation can be expressed as

$$\frac{d}{dr}\left(r^2\frac{dT_{gas}}{dr}\right)=Z\frac{dT_{gas}}{dr} \quad \text{where} \quad Z\equiv\frac{\dot{m}c_{p,gas}}{4\pi k_{gas}} \quad . \tag{48}$$

Integrating Eq. 48 using the boundary conditions,

$$T(r\to\infty)=T_\infty \quad \text{and} \quad T(r_s)=T_b \quad , \tag{49}$$

where r_s is the droplet surface radius and T_b is the hydrocarbon boiling temperature, gives the gas-phase temperature distribution,

$$T(r)=\frac{(T_\infty-T_b)\exp(-Z/r)-T_\infty\exp(-Z/r_s)+T_b}{1-\exp(-Z/r_s)} \quad . \tag{50}$$

The droplet surface energy balance is presented in Fig. 1 and can be expressed as

$$\dot{m}\left(h_{fg,LH}+\int_{T_{init}}^{T_{boil}}c_{p,LH}dT\right)=q_{cond} \tag{51}$$

where q_{cond} is the heat conducted from the gas-phase to the droplet, $h_{fg,LH}$ is the hydrocarbon enthalpy of vaporization and $c_{p,LH}$ is the liquid hydrocarbon specific heat. Using Fourier's law for q_{cond}, Eq. 51 becomes

$$\dot{m}\left(h_{fg,LH}+\int_{T_{init}}^{T_{boil}}c_{p,LH}dT\right)=4\pi k_{gas}r_s^2\left.\frac{dT}{dr}\right|_{r_s} \tag{52}$$

Substituting the gas-phase temperature gradient, dT/dr, at the droplet surface and solving for $\dot{m}$, yields

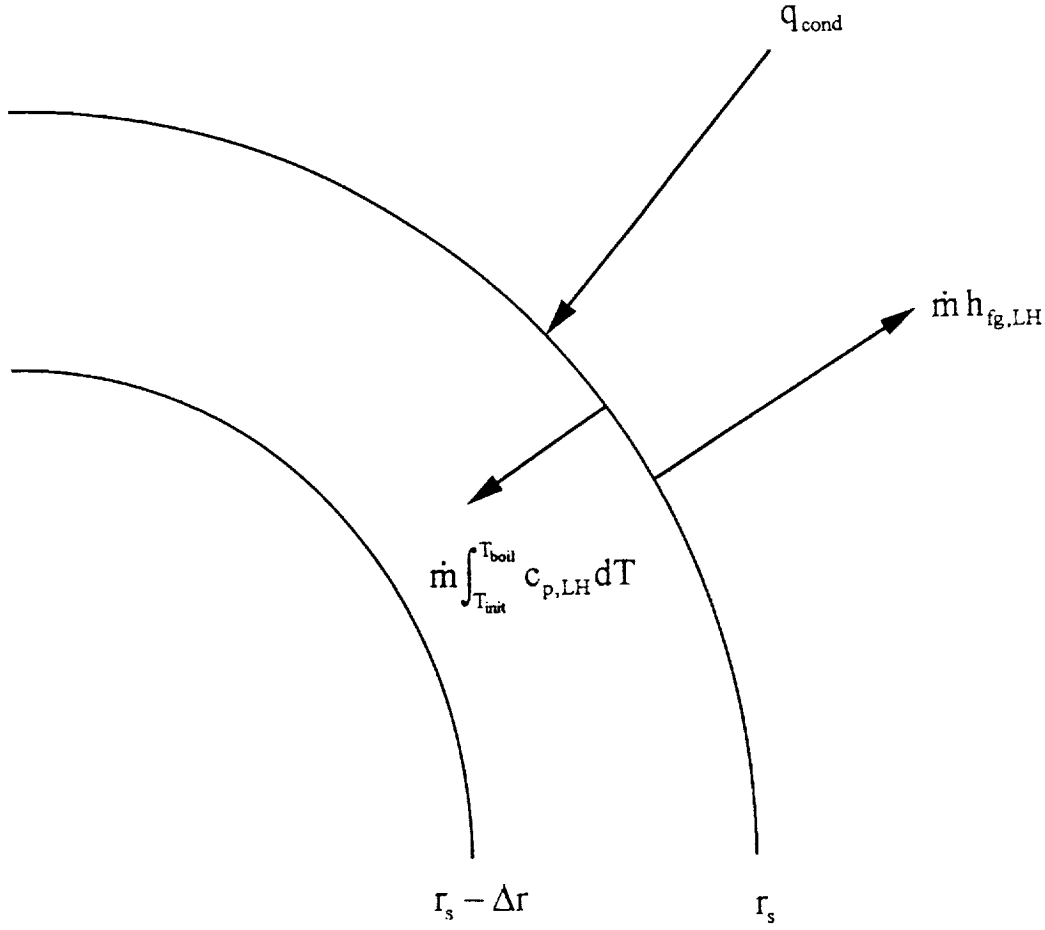

Figure 1. Surface energy balance for liquid hydrocarbon droplet with heat up of thin liquid layer between r_s-Δr and r_s from initial temperature to boiling temperature.

$$\dot{m} = \frac{4\pi k_{gas} r_s}{c_{p,gas}} \ln\left[\frac{c_{p,gas}(T_\infty - T_b)}{h_{fg,LH} + \int_{T_{init}}^{T_{boil}} c_{p,LH}\,dT} + 1\right] \quad . \tag{53}$$

Writing a mass balance for the droplet produces the following result:

$$\frac{dm_{drop,LH}}{dt} = -\frac{4\pi k_{gas} r_s}{c_{p,gas}} \ln\left[\frac{c_{p,gas}(T_\infty - T_b)}{h_{fg,LH} + \int_{T_{init}}^{T_{boil}} c_{p,LH}\,dT} + 1\right] \tag{54}$$

which is used in the system mass and energy governing equations.

Aluminum Combustion: As mentioned previously, aluminum combustion proceeds through two different oxidation mechanisms; the first is aluminum vapor oxidation, and the second is droplet surface condensation/oxidation. This dual process phenomena requires a complex model for accurate results. Work is in progress to incorporate a detailed aluminum combustion model[17,23] in the combustor code. However, the aluminum combustion process is currently treated using a simple combustion model. In this model, all heat released by surface oxidation/condensation goes into the droplet with none lost to the gases surrounding the droplet. The following assumptions are also used:

- Quasi-steady droplet evaporation
- Uniform droplet temperature equal to aluminum boiling temperature
- Lewis number, Le = 1
- Al_2O_3 surface agglomeration does not interfere with aluminum vaporization
- Constant thermophysical properties

The gas-phase sensible energy balance is similar to that of the hydrocarbon droplet yielding a gas temperature distribution,

$$T(r) = \frac{(T_f - T_b)\exp(-Z/r) - T_\infty \exp(-Z/r_s) + T_b}{1 - \exp(-Z/r_s)} \quad , \qquad (55)$$

where Z and r_s now apply to the aluminum droplet and T_f is the aluminum flame temperature.

However, the droplet surface energy balance is modified by the condensation of Al_2O_3 on the surface. A schematic of the energy balance is presented in Fig. 2. Employing the assumption that all heat produced by the condensation/oxidation reaction goes into the droplet yields

$$\dot{m}_{Al} h_{fg,Al} = q_{c,gas} + \dot{m}_{Al_2O_3} h_{fg,Al_2O_3} \quad , \qquad (56)$$

where $\dot{m}_{Al_2O_3}$ is the rate at which Al_2O_3 condenses on the droplet surface. The Al_2O_3 condensation rate, $\dot{m}_{Al_2O_3}$, can be expressed as a fraction, η, of the aluminum vaporization rate, $\dot{m}_{Al}$. Substituting $\eta\dot{m}_{Al}$ for $\dot{m}_{Al_2O_3}$ and rearranging Eq. 56 produces

$$\dot{m}_{Al}\left(h_{fg,Al} - \eta h_{fg,Al_2O_3}\right) = q_{c,gas} \quad . \qquad (57)$$

A value of $\eta = 0.4$ was determined from previous aluminum combustion work involving both experimental and numerical analyses.[17]

Substituting Fourier's law for $q_{c,gas}$ as was done for the hydrocarbon and solving for $\dot{m}_{Al}$ yields the following:

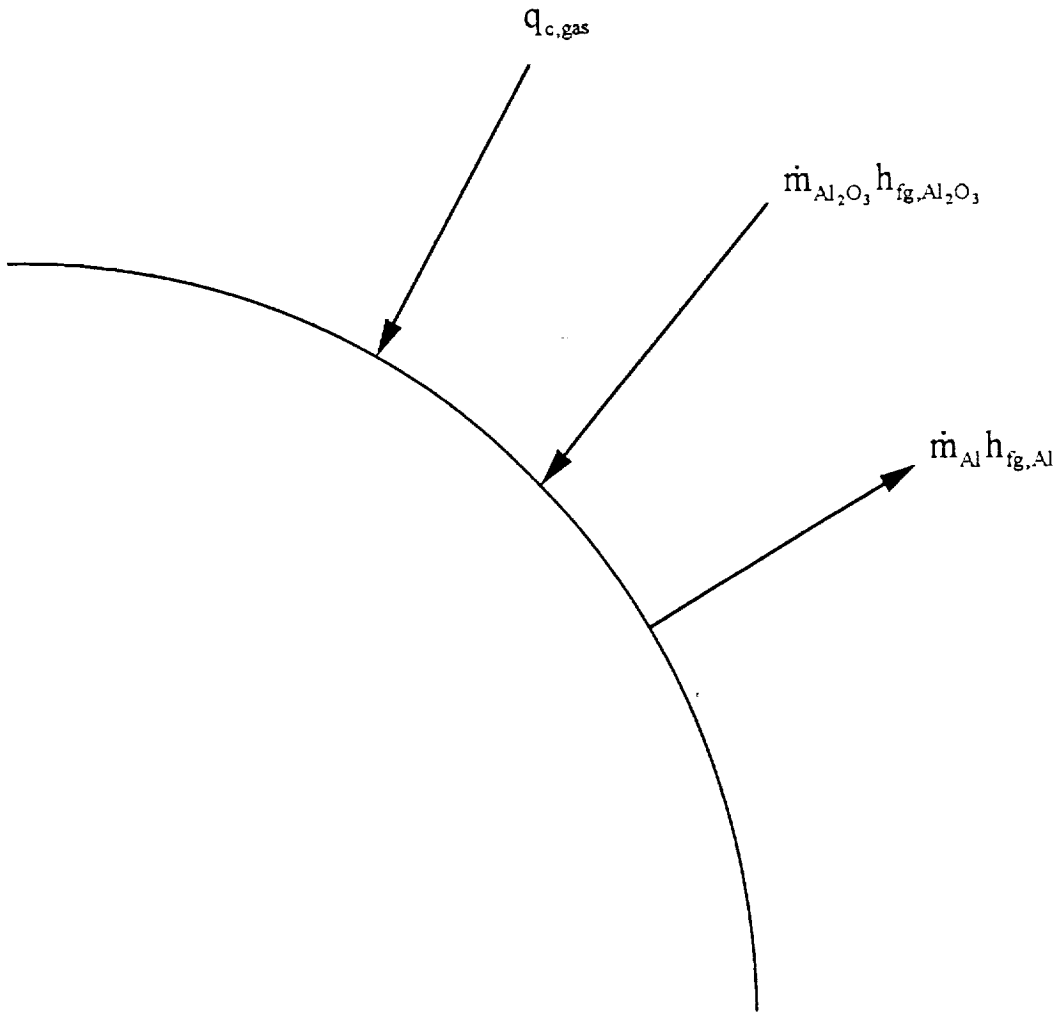

Figure 2. Surface energy balance for liquid aluminum droplet with heat transfer from oxide agglomerate condensing on the droplet surface.

$$\dot{m}_{Al} = \frac{4\pi k_{gas} r_s}{c_{p,gas}} \ln\left[\frac{c_{p,gas}(T_f - T_b)}{\left(h_{fg,Al} - \eta h_{fg,Al_2O_3}\right)} + 1\right] \quad . \tag{58}$$

Mass conservation for the aluminum droplet can be expressed as

$$\frac{dm_{drop,Al}}{dt} = -\frac{4\pi k_{gas} r_s}{c_{p,gas}} \ln\left[\frac{c_{p,gas}(T_f - T_b)}{\left(h_{fg,Al} - \eta h_{fg,Al_2O_3}\right)} + 1\right] \quad . \tag{59}$$

It should be noted that h_{fg,Al_2O_3} is not a true enthalpy of vaporization since Al_2O_3 does not exist in a gaseous state. Rather, it dissociates into $2Al + 3/2O_2$. Therefore h_{fg,Al_2O_3} is actually the enthalpy released by the chemical reaction, $2Al_{(g)} + 3/2O_2 \rightarrow Al_2O_{3(l)}$, occurring at the droplet surface temperature.

In both the hydrocarbon and the aluminum droplet models, the thermophysical properties, c_p and k_{gas}, are assumed to be constant. However, both of these properties are actually functions of gas temperature, which varies with radius from the droplet surface to the ambient gas environment. Thus, it is necessary to determine an average value for c_p and k_{gas}. Following the work of Law and Williams[24], the following values of c_p and k_{gas} are used:

$$\begin{aligned} c_{pg} &= c_{pf}(\overline{T}) \\ k_{gas} &= 0.4k_f(\overline{T}) + 0.6k_\infty(\overline{T}) \end{aligned} \tag{60}$$

where $T = (T_b + T_\infty)/2$. In the above equations, the subscript f denotes the gaseous fuel property, either hydrocarbon or aluminum.

Solution Method

Equations 13, 22, 44, 54, and 59 form the governing equation set and are numerically integrated in the axial direction using the IMSL Dverk integration routine[25] to determine $\dot{m}_g$, $(\dot{m}h)_g$, u_p, $\dot{m}_{LH}$, $\dot{m}_{Al}$, and $\dot{m}_{Al_2O_3}$. These values are then used to determine the gas temperature, $T_g(x)$, the radiation heat flux, $q(x)$, final Al_2O_3 agglomerate diameter, and chamber burnout length. Initial conditions are supplied at the injector face. The solution of these equations requires the knowledge of the following properties at each solution point:

- Gas-phase T, ρ, μ and k
- Liquid hydrocarbon h, h_{fg}, ρ, and T_b
- Vapor-phase hydrocarbon k and c_p
- Liquid aluminum h, h_{fg}, ρ, and T_b
- Vapor-phase aluminum k and c_p
- Al_2O_3 agglomerate h at $T_{b,Al}$, and ρ

Physical Properties

Gas-phase temperature, density, and composition are calculated using the STANJAN chemical equilibrium subroutine.[26] Temperature-dependent gas-phase conductivity and viscosity are currently approximated as those of O_2 using third-order polynomial curve fits of Svhela's tabulations.[13] Coefficients and valid temperature ranges are presented in Tables Ia and Ib.

The gas mixture is approximated as a single gas because of the complexities of calculating gas mixture properties. Gas species interactions must be accounted for to accurately determine these properties. In the future, gas-phase conductivity and viscosity will be calculated using a property subroutine that accounts for these mixture effects.

Table I a. O_2 Conductivity, $k = A + BT + CT^2 + DT^3$ (W/m·K)				
A	B	C	D	Temp Range (K)
9.6789×10^{-4}	9.6973×10^{-5}	-3.3806×10^{-8}	1.072×10^{-11}	100 - 1000
-9.8981×10^{-3}	1.2178×10^{-4}	-4.8×10^{-8}	1.0847×10^{-11}	1000 - 1500
3.016×10^{-2}	3.888×10^{-5}	9.2148×10^{-9}	-2.3244×10^{-12}	1500 - 2000
1.0799×10^{-3}	8.4393×10^{-5}	-1.4793×10^{-8}	1.937×10^{-12}	2000 - 2500
6.791×10^{-2}	4.6007×10^{-6}	1.7085×10^{-8}	-2.3244×10^{-12}	2500 - 3000
-3.3408×10^{-2}	1.0636×10^{-4}	-1.7201×10^{-8}	1.5496×10^{-12}	3000 - 3500
1.4209×10^{-1}	-4.0726×10^{-5}	2.4058×10^{-8}	-2.3244×10^{-12}	3500 - 4000

Table I b. O_2 Viscosity, $\mu = A + BT + CT^2 + DT^3$ (kg/m·s)·10^6				
A	B	C	D	Temp Range (K)
4.5863	6.0007×10^{-2}	-2.0733×10^{-5}	4.2703×10^{-9}	300-2000 K
16.601	3.5227×10^{-2}	-3.3703×10^{-6}	2.2687×10^{-10}	2000-4000 K

This property subroutine has already been developed for previous work in modeling single aluminum droplet combustion.[17]

The JP-10 properties (ρ, c_p, h_{fg}, and T_b) are taken from Szekely.[27] Liquid JP-10 density was determined as

$$\rho_{JP-10} = 1166.4 - 0.792T(K) \quad kg/m^3 \quad . \tag{61}$$

Similarly, liquid specific heat was correlated as

$$c_p = 257.32 + 4.5187 \cdot T(K) \quad J/kg \cdot K \quad . \tag{62}$$

JP-10 boiling temperature was determined from the following curvefit of temperature as a function of vapor pressure:

$$T = \frac{-4704.2}{\ln\left(P(Pa)/3.069 \times 10^9\right)} \quad K \quad . \tag{63}$$

By setting the pressure equal to chamber pressure, Eq. 63 yields the boiling temperature. Presently, the enthalpy of vaporization as a function of chamber pressure is unknown. Therefore, the enthalpy of vaporization at 1 atm will be used until a more accurate enthalpy is determined. Using the Clausius-Clapeyron relationship, Szekely[27] found the JP-10 enthalpy of vaporization to be

$$h_{fg,JP-10} = 286.7 \text{ kJ/kg} \quad . \tag{64}$$

The liquid aluminum properties (h, h_{fg}, and T_b) are determined from the JANAF tables[28], as developed below, and gaseous aluminum properties (c_p and k) are curvefits of Svehla's tabulations[13], presented in Tables IIa and IIb.

Table II a.

Gaseous Al specific heat, $c_p = A + BT + CT^2 + DT^3$ (J/kg·K)

A	B	C	D	Temp Range (K)
787.78	-3.0233×10^{-2}	1.8608×10^{-5}	-3.8859×10^{-9}	600 - 2000
770.65	0.0	0.0	0.0	2000 - 3000
686.07	8.0895×10^{-2}	-2.6181×10^{-5}	2.8731×10^{-9}	3000 - 4000

Table II b.

Gaseous Al conductivity, $k \cdot 10^6 = A + BT + CT^2 + DT^3$ (W/m·K)

A	B	C	D	Temp Range (K)
7.5771	5.9643×10^{-2}	-7.1434×10^{-7}	2.0696×10^{-14}	600 - 1000
5.4714	6.6217×10^{-2}	-8.8889×10^{-6}	3.7037×10^{-9}	1000 - 1500
45.594	-1.0946×10^{-2}	4.1389×10^{-5}	-7.4074×10^{-9}	1500 - 2000
60.12	-1.7836×10^{-2}	3.7499×10^{-5}	-5.5555×10^{-9}	2000 - 2500
19.527	3.7058×10^{-2}	1.2778×10^{-5}	-1.8519×10^{-9}	2500 - 3000
-109.19	0.1627	-2.869×10^{-5}	2.7778×10^{-9}	3000 - 3500
-121.0	0.15855	-2.3333×10^{-5}	1.8519×10^{-9}	3500 - 4000

The JANAF tables provide the specific enthalpy of both liquid and gaseous aluminum over a significant temperature range, permitting the aluminum enthalpy of vaporization, $h_{fg,Al}$, to be calculated over the temperature range. The following third-order polynomial curve fit for $h_{fg,Al}$ was then determined:

$$h_{fg,Al} = 11.905 \times 10^6 - 400.59T - 2.4365 \times 10^{-3} T^2 + 3.4091 \times 10^{-7} T^3 \quad J/kg \tag{65}$$

and substituted into the Clausius-Clapeyron relationship,

$$\left.\frac{dP}{dT}\right|_{sat} = \frac{h_{fg}}{Tv_{fg}} \quad . \tag{66}$$

Assuming that the vapor specific volume, v_g, is much larger than the liquid specific volume, v_l, and that the vapor behaves as an ideal gas, the Clausius-Clapeyron relationship can be expressed as

$$\left.\frac{dP}{dT}\right|_{sat} = \frac{P}{RT^2}\left(11.905 \times 10^6 - 400.59T - 2.4365 \times 10^{-3} T^2 + 3.4091 \times 10^{-7} T^3\right) \quad , \tag{67}$$

where P is saturation pressure, T is saturation temperature, and R is the specific gas constant. Rearranging and integrating yields the following expression:

$$R \ln\left(\frac{P_2}{P_1}\right) = -11.905 \times 10^6 \left[\frac{1}{T_2} - \frac{1}{T_1}\right] - 400.39\left[\ln\left(\frac{T_2}{T_1}\right)\right] - 2.4365 \times 10^{-3}\left[T_2 - T_1\right] + 1.7045 \times 10^{-7}\left[T_2^2 - T_1^2\right] \quad . \tag{68}$$

Substituting the known saturation conditions, P_{sat} = 1 atm, and T_{sat} = 2790.812 K, for P_1 and T_1 in Eq. 68 provides a relationship for the saturation pressure, P_2, as a function of T_2. However, Equation 68 cannot be rearranged to yield T_2 as a function of P_2. Therefore, T_2 is determined through a Newton-Raphson solution of Eq. 68. If a given saturation pressure, P_2, is equal to the combustion chamber pressure, then the corresponding temperature, T_2, is the aluminum boiling temperature. Once $T_{b,Al}$ has been found, $h_{fg,Al}$ is determined from Eq. 65.

The liquid aluminum specific enthalpy, h_{Al}, is determined through a third-order polynomial curvefit of JANAF data, resulting in the following expression:

$$h_{Al} = -29467 + 1177.5T + 4.5106 \times 10^{-5} T^2 - 5.1928 \times 10^{-9} T^3 \quad (J/kg). \tag{69}$$

We assume the Al_2O_3 agglomerate temperature is equal to the aluminum boiling temperature as long as aluminum is present in the droplet, after which the Al_2O_3 agglomerate is free to equilibrate with the gas flow temperature. Therefore, the Al_2O_3 agglomerate should exist only in the molten state in the combustion chamber since the Al_2O_3 melting temperature (T_m = 2315 K) is much less than both the aluminum boiling temperature ($T_b \geq$ 2790 K) and the gas temperature once the aluminum is consumed. Following the work of Kirshenbaum and Cahill[29], the molten Al_2O_3 density, $\rho_{Al_2O_3}$, is modeled as:

$$\rho_{Al_2O_3} = 5632 - 1.127T(K) \quad kg/m^3 \quad . \tag{70}$$

The liquid Al_2O_3 enthalpy is determined through a third-order polynomial curvefit of JANAF data:

$$h_{Al_2O_3} = 1.504d7 + 839.01T + 0.23354T^2 - 3.0298 \times 10^{-5} T^3 \quad (J/kg) \; . \tag{71}$$

Theoretical Results

The one-dimensional engine code was exercised using the chamber diameter, pressure, flow rates, and aluminum mass loading presented in Table III. These values were chosen to simulate Galecki's test conditions.[8] Presently, chamber length is varied to allow complete propellant combustion.

Table III.
Model Operating Conditions

Chamber Diameter	0.0522 m
Chamber Pressure	690 kPa
Slurry Flow Rate	0.00142 kg/s
Aluminum Loading	60%
Oxidizer Flow Rate	0.00312 kg/s

A normalized droplet size distribution remains to be determined from other researchers' work on slurry atomization. A literature search has been started to find appropriate references on this topic. For the present time, the arbitrary normalized size distribution in Fig. 3 is used.

Secondary atomization effects on combustion chamber gas and droplet velocities can be seen in Figs. 4 and 5. The data in Fig. 4 were calculated assuming no secondary atomization while the data in Fig. 5 assume a fragmentation ratio, β, of 40. In both cases, smaller droplets equilibrate more rapidly with the gas velocity than large droplets, and the gas velocity increases along the combustor axis due to decreasing gas density as temperature rises and mass addition to the gas flow from the slurry droplets.

As expected, droplet velocities are the same in both cases until secondary atomization occurs, after which, the slope of the Fig. 5 velocity profiles decreases sharply

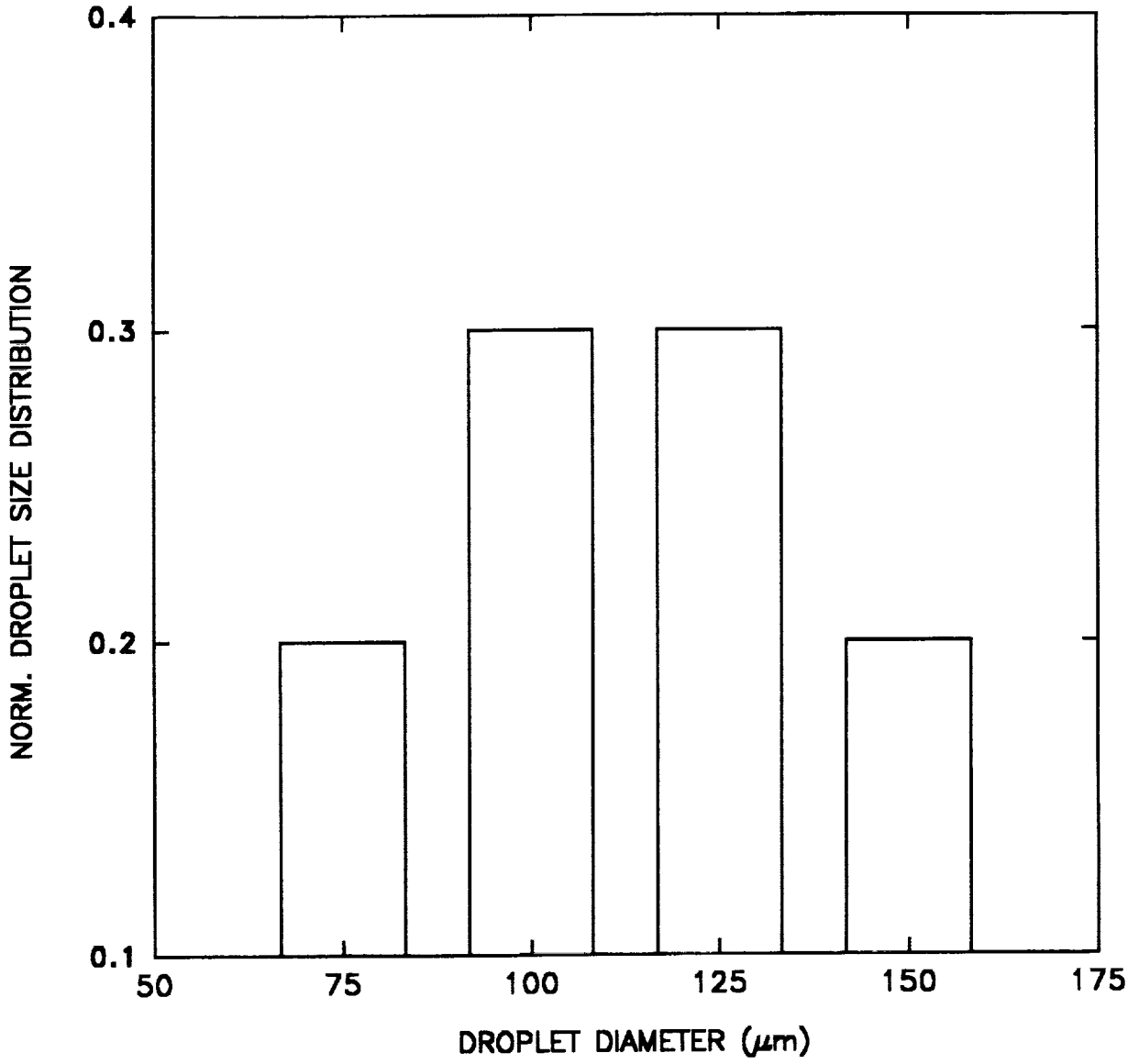

Figure 3. Normalized droplet size distribution used in combustor code.

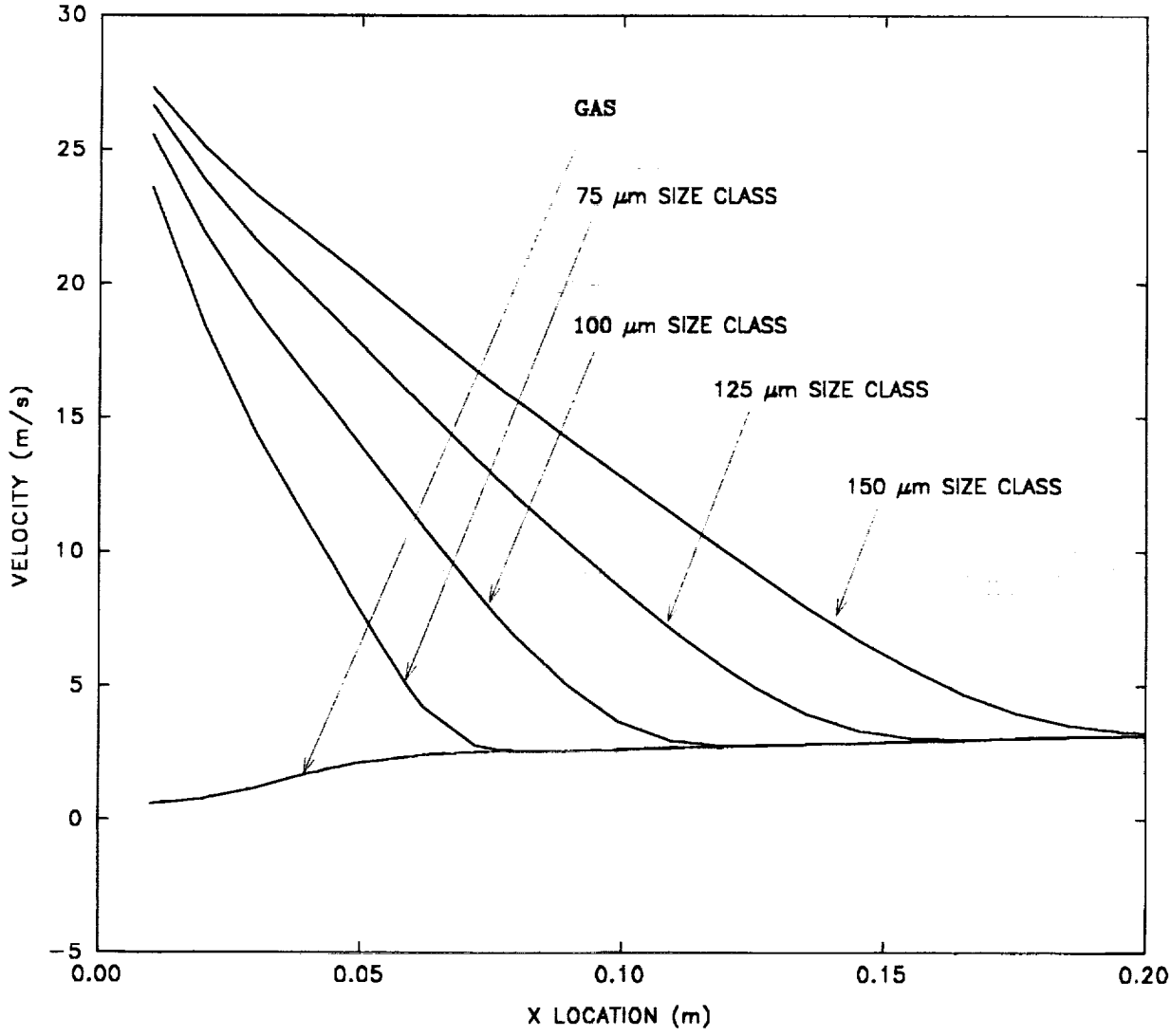

Figure 4. Gas and droplet velocities versus axial location for a 60 wt% Al slurry assuming no secondary atomization.

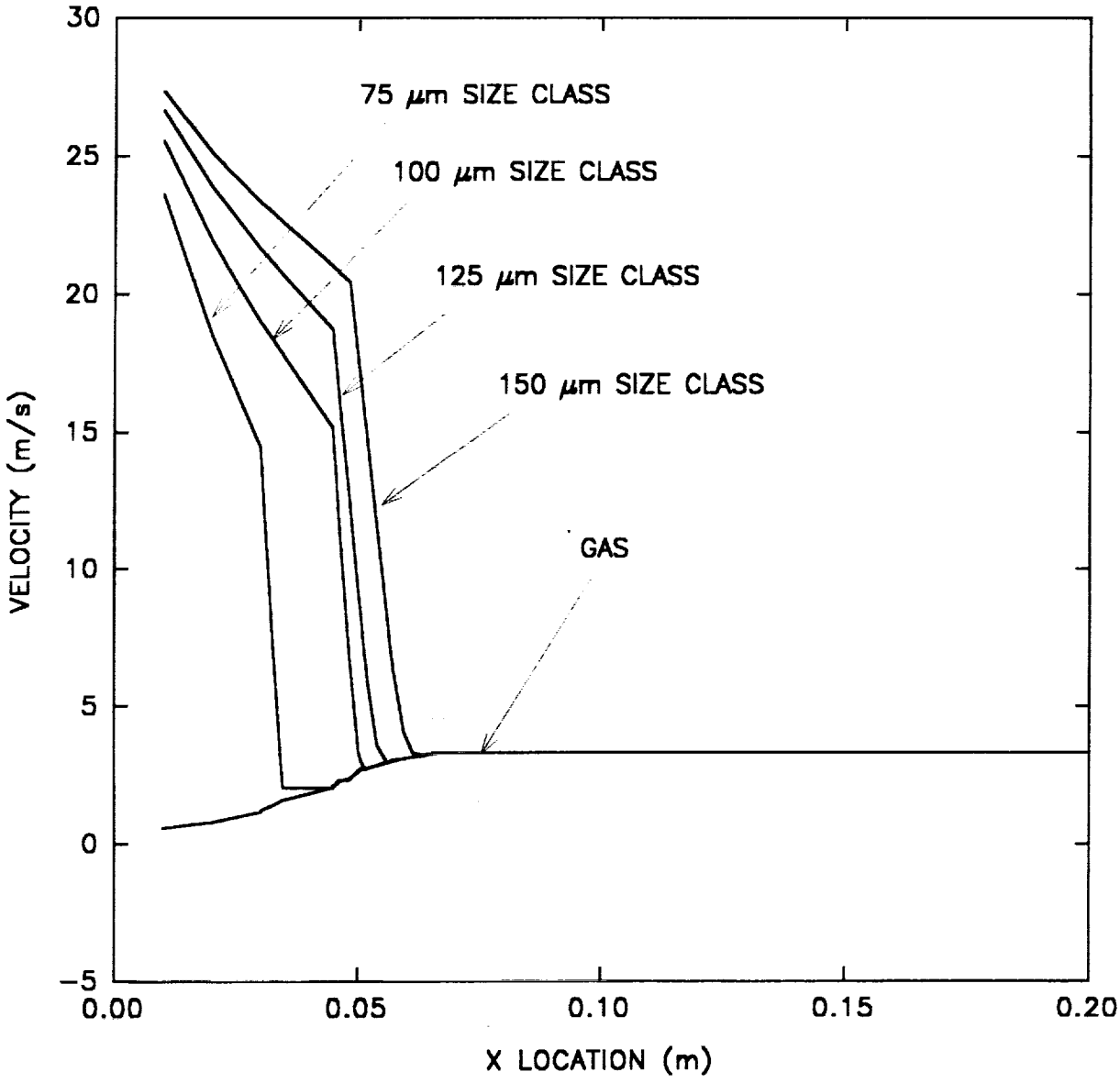

Figure 5. Gas and droplet velocities versus axial location for a 60 wt% Al slurry assuming a secondary atomization fragmentation ratio of 40.

and the droplet velocities rapidly equilibrate with the gas velocity. This rapid equilibration is caused by secondary atomization shattering the initial droplets into small secondary droplets which equilibrate with the gas velocity more quickly than the initial droplet could.

Typical major and minor gas flow species mass fractions are presented in Figs. 6 and 7, respectively. Again, a fragmentation ratio of 40 was used in calculating the data in both of these figures. The jagged shape of the mass fraction curves can be attributed to secondary atomization effects on burning rates and the sudden extraction of enthalpy from the gas flow to account for aluminum heat up. This second effect will be eliminated upon the addition of a proper aluminum heat up model.

From Fig. 6, it is seen that the O_2 mass fraction decreases steadily as droplet combustion progresses. However, the flow is oxidizer rich, resulting in excess O_2 upon fuel burnout. CO_2 and H_2O mass fractions reach maximums at approximately 0.04-0.05 m and then decrease as increasing temperature causes dissociation, evidenced by increasing CO and OH mass fractions in Figs. 6 and 7. It should also be noted that the liquid Al_2O_3 mass fraction of 0.25 is much greater than the solid Al_2O_3 mass fraction of 0.02.

Gas temperature versus axial location for the same conditions is plotted in Fig. 8. The maximum gas temperature of 3872 K is only slightly higher than the 3829 K predicted for equilibrium. This difference is attributed to the Al_2O_3 oxide agglomerate temperature being fixed at the Al boiling point instead of being permitted to equilibrate with the gas temperature. Work is currently in progress to incorporate this equilibration process in the combustor model.

In Fig. 9, chamber burnout distance is plotted versus fragmentation ratio, β, to illustrate the benefits of secondary atomization. It is readily apparent that only slight secondary atomization is required to yield significant decreases in droplet lifetimes. Higher secondary atomization intensities, represented by larger fragmentation ratios, have a lesser effect on burnout length because droplet lifetime is inversely proportional to

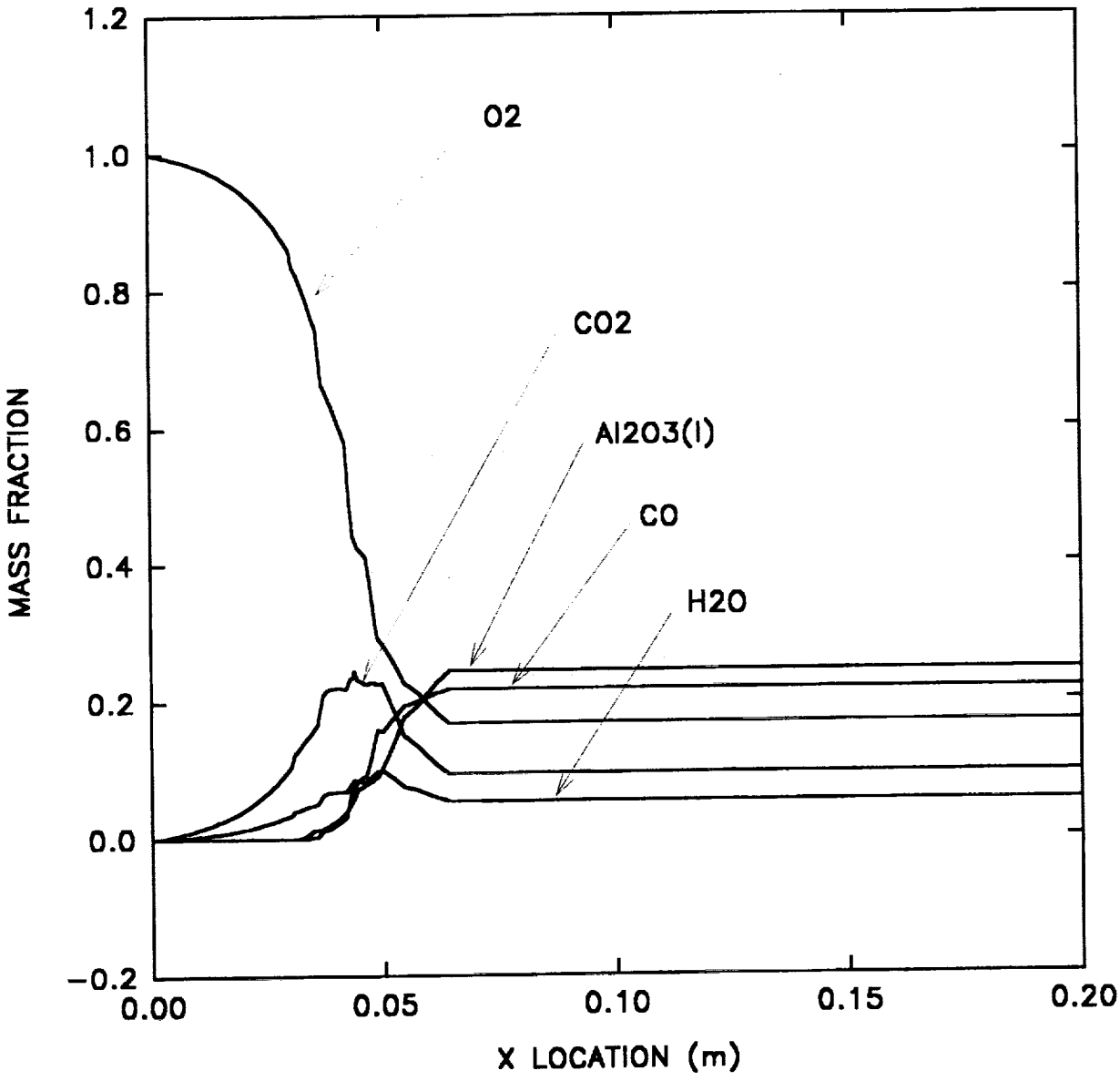

Figure 6. Mass fraction of major gas species versus axial location. Data is for a 60 wt% Al slurry assuming a secondary atomization fragmentation ratio of 40.

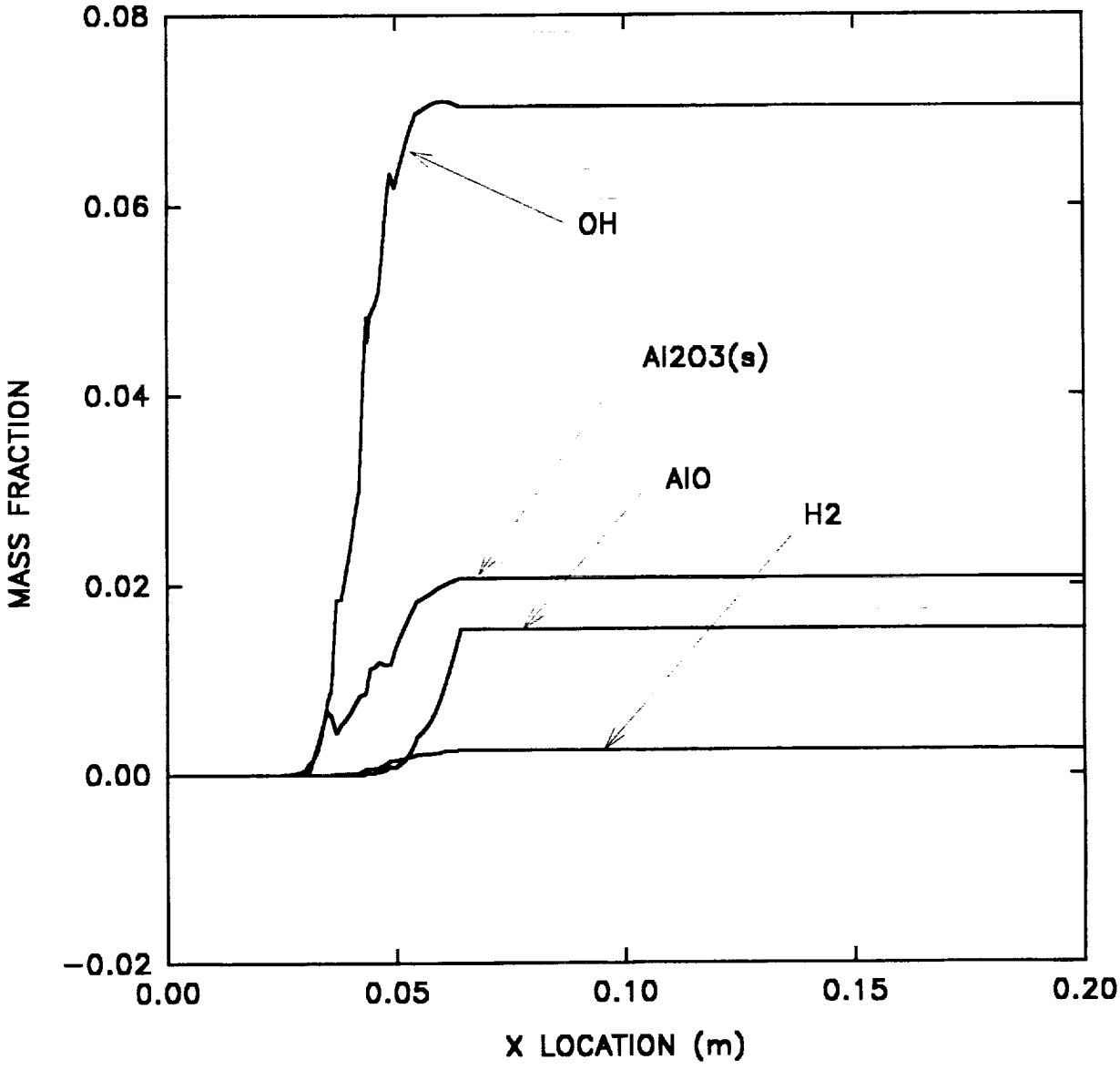

Figure 7. Mass fraction of minor gas species versus axial location for a 60 wt% Al slurry assuming a secondary atomization fragmentation ratio of 40.

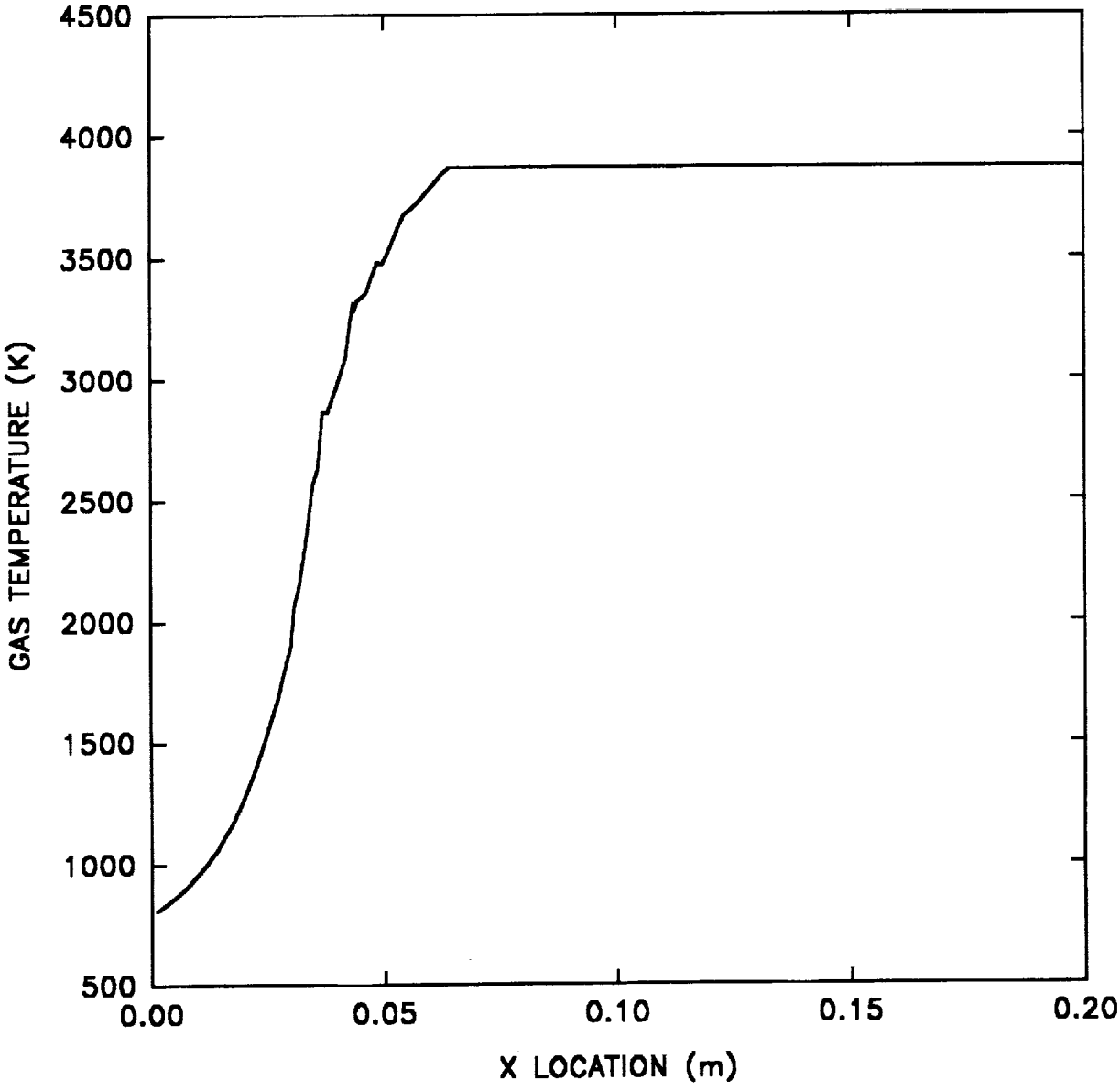

Figure 8. Gas temperature versus axial location for a 60 wt% Al slurry assuming a secondary atomization ratio of 40.

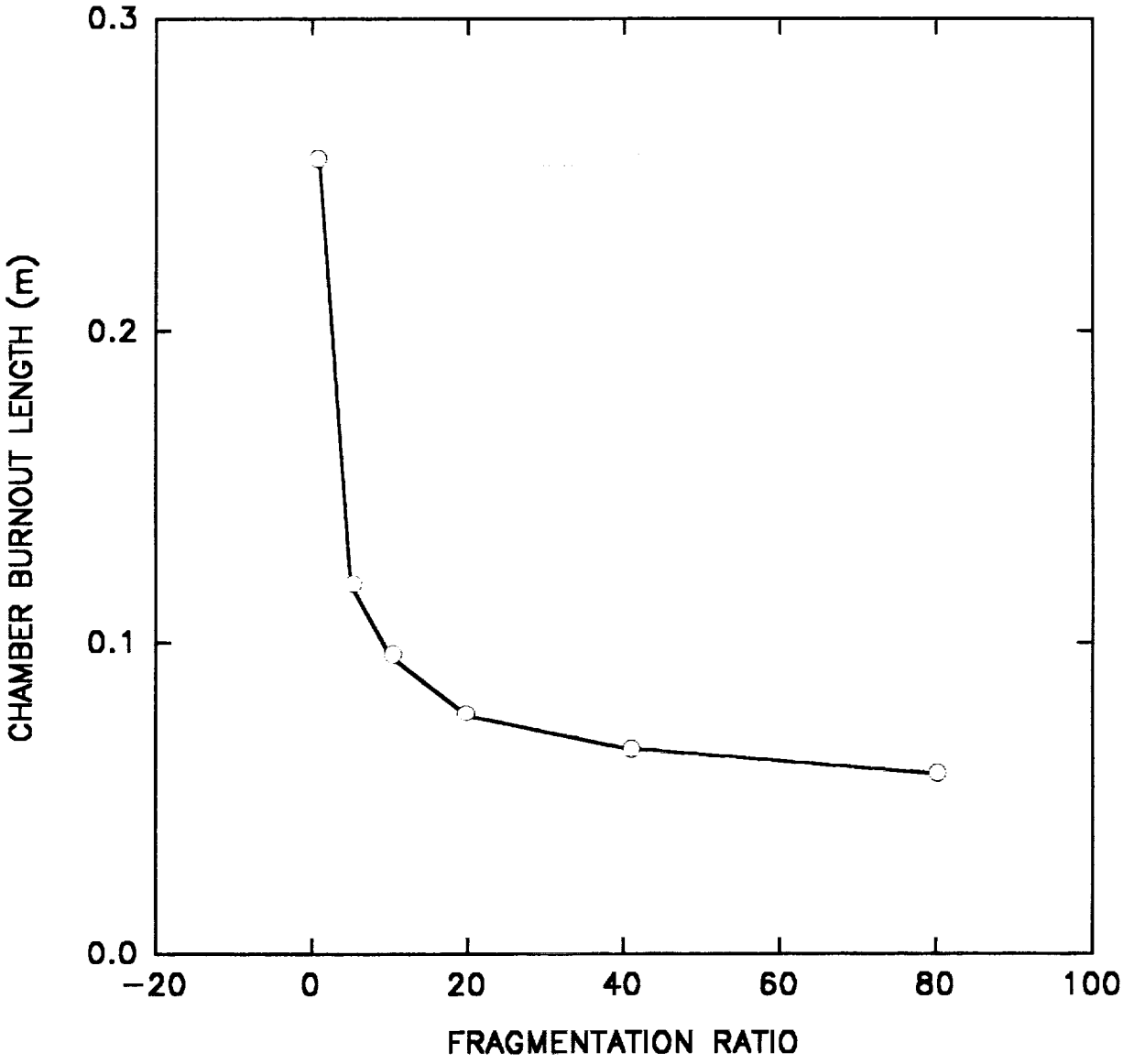

Figure 9. Chamber burnout distance as a function of secondary atomization fragmentation ratio for a 60 wt% Al slurry.

droplet surface area, which increases as $(\beta)^{2/3}$. It should be emphasized that the burnout distances presented in Fig. 9 neglect the Al agglomerate heat up which is likely to increase these distances significantly .

Final oxide agglomerate diameter as a function of secondary atomization intensity, β, is shown in Fig. 10. Similar to the trend seen in Fig. 9, small secondary atomization intensities significantly reduce final Al_2O_3 agglomerate diameters, with greater atomization intensities providing decreasing marginal reductions in diameter. However, final particle diameter is proportional to $(1/\beta)^{1/3}$ and not $(1/\beta)^{2/3}$ as was droplet lifetime.

The results presented in Figs. 4-10 demonstrate that the combustor model is performing as expected, given current model assumptions, and that only low secondary atomization intensities are required to significantly decrease chamber burnout length and final particle size.

Experimental Efforts

The main focus of our work during this reporting period was devoted to the theoretical model development described above. Experimental efforts consisted of improvements to the experimental apparatus described in earlier reports[30-33]. Previously, the transmitting and receiving optics were mounted on separate optical tables that were not isolated from the floor. Building vibrations and people moving about the lab were sufficient to distort optical alignment.

To correct this problem, both optical table tops and the burner were mounted on a single frame constructed of steel box beams. The entire assembly was then mounted on five isolation legs (Newport pneumatic isolation mount type XL-A). The optics were reassembled and the setup was recalibrated. Shakedown tests indicate that the system is correctly calibrated and that the apparatus is now sufficiently isolated from vibrations.

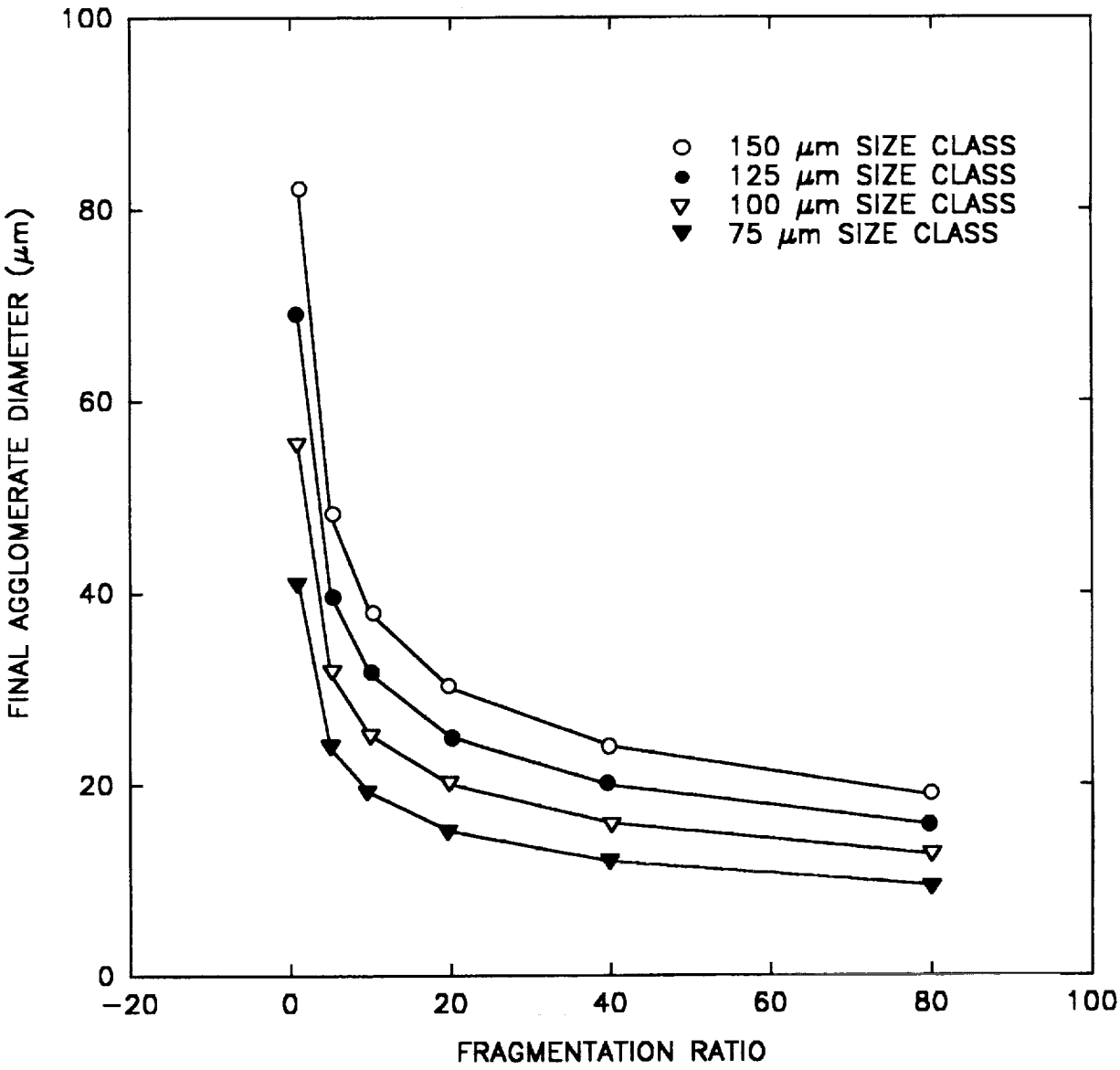

Figure 10. Final oxide agglomerate diameter as a function of secondary atomization fragmentation ratio. Data is for a 60 wt% Al slurry.

Future Plans

Plans for the next six months include the following:

1. Incorporate Al heat up, gas mixture properties, radiation heat transfer, and improved aluminum combustion model in the one-dimensional rocket code.

2. Determine whether existing rocket nozzle codes are suitable for modeling the expansion of slurry combustion products. If not, develop a one-dimensional nozzle code incorporating two-phase flow losses.

3. Begin characterizing slurry and secondary atomization effects on engine performance.

4. Examine role of surfactants in secondary atomization by adding additional surfactants to existing slurries.

5. Continue investigating the sample volume size probability distribution function and its sensitivity to particle index of refraction.

6. Use existing experimental apparatus and additional imaging techniques to resolve post-secondary atomization droplet size distributions.

References

1. Palaszewski, B.A., "Lunar Missions Using Advanced Chemical Propulsion: System Design Issues," AIAA Paper 90-2431, July 1990.

2. Palaszewski, B.A., "Metallized Propellants for the Human Exploration of Mars," NASA Technical Paper 3062, Nov. 1990.

3. Palaszewski, B.A., "Advanced Launch Vehicle Upper Stages Using Liquid Propulsion and Metallized Propellants," NASA Technical Memorandum 103622, Oct. 1990.

4. Zurawski, R.L., and Green, J.M., "An Evaluation of Metallized Propellants Based on Vehicle Performance," AIAA Paper 87-1773, June-July 1987.

5. Rapp, D.C., "High Energy-Density Liquid Rocket Fuel Performance," AIAA Paper 90-1968, July 1990.

6. Wong, S.-C., and Turns, S.R., "Disruptive Burning of Aluminum/Carbon Slurry Droplets," *Combust. Sci. and Tech.*, Vol. 66, 1989, pp. 75-92.

7. Mueller, D.C., Scott, M.J., and Turns, S.R., "Secondary Atomization of Al/RP-1 Liquid Rocket Slurry Fuels," AIAA Paper 91-3625, Sept 1991.

8. Galecki, D.L., "Ignition and Combustion of Metallized Propellants," AIAA Paper 89-2883, July 1989.

9. Kraeutle, K.J., "Particle Size Analysis in Solid Propellant Combustion Research," *Progress in Astronautics and Aeronautics*, Vol. 53, 1977, pp. 449-463.

10. Salita, M., "Quench Bomb Investigation of Al_2O_3 Formation From Solid Rocket Propellants (Part II): Analysis of Data," *25th JANNAF Combustion Meeting*, Oct. 1988, pp. 185-197.

11. Dobbins, R.A., and Strand, L.D., "A Comparison of Two Methods of Measuring Particle Size of Al_2O_3 Produced by a Small Rocket Motor," *AIAA Journal*, Vol. 8, No. 9, Sept. 1970, pp. 1544-1550.

12. Parry, D.L., and Brewster, M.Q., "Optical Constants of Al_2O_3 Smoke," *Journal of Thermophysics*, Vol. 5, April-June 1991, pp. 142-149.

13. Svehla, R.A., "Estimated Viscosities and Thermal Conductivities of Gases at High Temperatures", NASA Technical Report R132, 1962.

14. Konopka, W.L., Reed, R.A., and Calia, V.S., "Measurements of Infrared Optical Properties of Al_2O_3 Rocket Particles," *Progress in Astronautics and Aeronautics*, Vol. 91, AIAA, New York, 1984, pp. 180-196.

15. Incropera, F.P., and DeWitt, D.P., Fundamentals of Heat and Mass Transfer - Third Edition, John Wiley and Sons, New York, 1990.

16. Wong, S.-C., and Turns, S.R., "Ignition of Aluminum Slurry Droplets," *Combust. Sci. and Tech.*, Vol. 52, 1987, pp. 221-242.

17. Turns, S.R., and Wong, S.-C., "Combustion of Aluminum-Based Slurry Agglomerates," *Combust. Sci. and Tech.*, Vol. 54, 1987, pp. 299-318.

18. Siegel, R., and Howell, J.R., Thermal Radiation Heat Transfer - Second Edition, Hemisphere Publishing Corp., New York, 1981, p. 498.

19. Kofink, W., "Complete Spherical Harmonic Solution of the Boltzmann Equation For Neutron Transport in Homogeneous Media With Cylindrical Geometry", *Nucl. Sci. and Eng.*, Vol. 6, 1959, pp. 475-486.

20. White, F.M., Viscous Fluid Flow, McGraw-Hill, New York, 1974, p. 209.

21. Cho, S.Y., Takahashi, F., and Dryer, F.L., "Some Theoretical Considerations on the Combustion and Disruption of Free Slurry Droplets", *Combust. Sci. and Tech.*, Vol. 67, 1989, pp. 37-57.

22. Takahashi, F., Heilweil, I.J., and Dryer, F.L., "Disruptive Burning Mechanism of Free Slurry Droplets", *Combust. Sci. and Tech.*, Vol. 65, 1989, pp. 151-165.

23. Law, C.K., "A Simple Theoretical Model for the Vapor-Phase Combustion of Metal Particles", *Combust. Sci. and Tech.*, Vol. 7, 1973, pp. 197-212.

24. Law, C.K., and Williams, F.A., "Kinetics and Convection in the Combustion of Alkane Droplets", *Combust. and Flame*, Vol. 19, 1972, pp. 393-405.

25. Anon., IMSL Library Reference Manual, IMSL, Inc., January 1, 1982.

26. Reynolds, W.C., "The Elemental Potential Method for Chemical Equilibrium Analysis: Implementation in the Interactive Program STANJAN," Department of Mechanical Engineering, Stanford University, January, 1986.

27. Szekely, G.A., "Experimental Evaluation of a Carbon Slurry Droplet Combustion Model", PhD Thesis, The Pennsylvania State University, 1982.

28. Stall, D.R., and Prophet, H., JANAF Thermochemical Tables, 2nd Ed., NSRDS-NBS 37, National Bureau of Standards, June 1971.

29. Kirshenbaum, A.D., and Cahill, J.A., "The Density of Liquid Aluminum Oxide," *Journal of Inorganic Nuclear Chemistry*, Vol. 14, 1960, pp. 283-287.

30. Turns, S.R., Mueller, D.C., and Scott, M.J., "Ignition and Combustion of Metallized Propellants- Semi-Annual Report," Grant No. NAG-3-1044, January 1990.

31. Turns, S.R., Mueller, D.C., and Scott, M.J., "Ignition and Combustion of Metallized Propellants- Semi-Annual Report," Grant No. NAG-3-1044, July 1990.

32. Mueller, D.C., and Turns, S.R., "Ignition and Combustion of Metallized Propellants- Semi-Annual Report," Grant No. NAG-3-1044, January 1991.

33. Mueller, D.C., and Turns, S.R., "Ignition and Combustion of Metallized Propellants- Semi-Annual Report," Grant No. NAG-3-1044, July 1991.